




Effects of variable deceleration periods on Rayleigh-Taylor instability with acceleration reversals

Denis Aslangil ¹, Andrew G. W. Lawrie ² and Arindam Banerjee ^{3,*}

¹*Department of Aerospace Engineering & Mechanics, The University of Alabama, Tuscaloosa, Alabama 35487, USA*

²*Department of Mechanical Engineering, University of Bristol, Queen's Building, University Walk, Clifton BS8 1TR, United Kingdom*

³*Department of Mechanical Engineering & Mechanics, Lehigh University, Bethlehem, Pennsylvania 18020, USA*



(Received 5 October 2021; accepted 17 May 2022; published 14 June 2022)

The dynamics of an interfacial flow that is initially Rayleigh-Taylor unstable but becomes statically stable for some intermediate period due to the reversal of the externally imposed acceleration field is studied. We discuss scenarios that consider both single and double-acceleration reversals. The *accel-decel* (AD) case consists of a single reversal imposed at an instant after the constant acceleration instability has entered a self-similar regime. The layer of mixed fluid ceases to grow upon acceleration reversal, and the dominant mechanics are due to internal wave oscillations. Variation of mass flux and the Reynolds stress anisotropy is observed due to the action of the internal waves. A second reversal of the AD case that is termed as *accel-decel-accel*, ADA is then explored; the response of the mixing layer is shown to depend strongly on the duration and the periodicity of the Reynolds stress anisotropy of the mixing layer during the deceleration period. We explore the effect of this variable deceleration period after the second acceleration reversal where the flow once again becomes Rayleigh-Taylor unstable based on metrics that include the integral mixing-layer width, bubble and spike amplitudes, mass flux, Reynolds stress anisotropy tensor, and the molecular mixing parameter.

DOI: [10.1103/PhysRevE.105.065103](https://doi.org/10.1103/PhysRevE.105.065103)

I. INTRODUCTION

The Rayleigh-Taylor instability (RT/RTI) develops at the interface of a heavy and light fluid when the system is subjected to an external acceleration field, $g(t)$ [1,2]. Classical RTI, where the acceleration remains constant, is a well-studied problem where a layer of turbulent mixing grows between the two pure fluids as initial perturbations to the interface develop into emergent vortical structures composed largely of pure fluids. The growth of these structures, labeled as spikes (heavy fluid penetrating the lighter fluid) and bubbles (light fluid penetrating the heavier fluid), and the self-similar growth can be characterized by [3,4]

$$h_{b,s} = \alpha_{b,s} A g t^2, \quad (1)$$

where $h_{b,s}$ is the height of the bubbles and spikes, $\alpha_{b,s}$ is the growth rate parameter, $A = \frac{(\rho_H - \rho_L)}{(\rho_H + \rho_L)}$ is the nondimensional density difference known as the Atwood number (where ρ_H and ρ_L are the densities of heavy and light fluids respectively), g is the acceleration, and t is the time. The evolution of hb and hs are similar for low Atwood numbers ($A < 0.1$); however, an asymmetry in h_b and h_s values are observed for larger A values, leading to faster-growing spikes [5–10]. RTI with constant acceleration occurs in combustion and chemical reaction processes, oceanic flows, weather inversions, and some forms of geological processes like salt-dome and volcanic-island formation [7,11,12]. The constant acceleration problem has been studied extensively; details can be found in recent comprehensive review articles [13–17].

However, the RTI problem is more complex in some natural and engineering applications, for example, in inertial confinement fusion (ICF) [18–20], and in blast waves of supernovae formations [21–23], where the instability is driven by a variable-acceleration $g(t)$ that is subjected to multiple reversals [24,25]. Studies that investigate acceleration reversals consist of a primary destabilizing acceleration of the system ($g > 0$) followed by an acceleration reversal to a stabilizing deceleration ($g < 0$) at a time t_1 , which in turn is followed by a second reversal at a time t_2 , leaving the system in another acceleration phase ($g > 0$). This acceleration history is known as *accel-decel-accel* or ADA [24–27]. This paper explores the distinct flow regimes on either side of acceleration reversals and the fundamental flow physics associated with them. Although the test cases we examine are not specific to ICF or supernovae, they are designed to understand the flow response to multiple acceleration reversals and the formation of relevant timescales observed by varying the deceleration phase. Such a canonical test case will not only allow us to better understand the flow and relevant physics in applications where RTI experience several acceleration reversals but also provide high-fidelity data for low-order model validation and verification under such scenarios. In short, the first acceleration reversal (deceleration phase) leads to a globally stable configuration, which cuts the flow of the pure fluids into the RTI mixing layer and thus increases the molecular mixing [26]. However, there remain unstable flow patches within the mixing layer where the flow is fully turbulent and well stirred, which leads to a form of dynamical behavior first observed in Ref. [27]. Such effects are, however, a short-term response of the large scales of the flow to the acceleration reversal. At time instants long after acceleration reversal, the

*arb612@lehigh.edu

flow still contains locally unstable patches due to residual turbulent motion within the mixing layer with observed oscillatory behavior in the Reynolds stress anisotropy tensor [27]; the oscillation properties were observed to be dependent on the initial conditions [27]. We attribute these oscillations to a form of internal wave occurring within the mixing layer.

In scientific literature, there has only been one experiment [26] and a small number of numerical simulations [24,25,27–31] that investigate the effects of variable acceleration on RTI. Dimonte and Schneider [26] employed a linear electric motor (LEM) to examine different acceleration histories using immiscible Freon and water ($A = 0.22$). They concluded that turbulent mixing was strongly dependent on the temporal acceleration profile $g(t)$ and may be important to ICF; however, mixing was minimized for impulsive acceleration profiles. In a follow-up publication, Dimonte *et al.* [24] compared data from previously unpublished moderate Atwood ($A = 0.48$) experiments with simulations using an implicit large-eddy simulation (ILES) solver [24]. Two different sets of initial conditions that promote bubble competition [24] were chosen: a broadband spectrum with modes 3–64 and an annular spectrum with modes 32–64; simulations with the broadband spectrum resembling the LEM experiments [26]. The authors observed that the acceleration reversal shredded previously formed bubble and spike structures under a stabilizing deceleration phase, resulting in near-complete mixing within that layer. Upon subsequent reacceleration, they found the instability recovers and returns nearly to its self-similar state. An increase in molecular mixing during the deceleration phase was also observed in direct numerical simulation studies of by Livescu *et al.* [30]. Ramaprabhu *et al.* [25] conducted both single- and multimode simulations using a massively parallel ILES solver, MOBILE. The single-mode simulations ($A = 0.15, 0.9$) demonstrate that the enhancement of mixing during the deceleration phase was directly related to Kelvin-Helmholtz vortices formed during the initial acceleration (growth) phase; those were, however, suppressed at larger Atwood numbers ($A = 0.9$). In the multimode simulations ($A = 0.5$), the authors observed a decrease in anisotropy tensor in the mixing layer during deceleration. Upon subsequent reacceleration, once transients associated with the conditions at reversal recede in significance, the anisotropy in the mixing layer recovers at late time to values consistent with the self-similar RTI with constant gravity.

Previous work by the authors [27] explored the effects of variation in initial conditions on the instability under multiple acceleration reversals. Similar to other studies [25], substantial anisotropy was observed during the deceleration period. In addition, oscillations in the anisotropy tensor were observed, leading the authors to hypothesize that internal waves oscillating inside the mixing layer led to the shredding of coherent structures in the mixed layer. Upon subsequent reacceleration, the flow recovered to exhibit self-similar behavior similar to constant-gravity RTI. It was concluded that the subsequent reacceleration phase might be considered akin to a classical RTI problem with an unusually thick interface which creates initial conditions in which a fraction of total energy is held as kinetic energy. The response to the acceleration reversal strongly depends on the spectral content of this thick interface.

Additional features of the acceleration-reversal problem have also been explored by Boffetta *et al.* [32], who conducted simulations using time-periodic rapid-acceleration reversals similar to a *Kapitza* pendulum. The resulting flow was found to freeze after a few periods of rapid reversals. A recent study by the authors explored RTI with varying periods of zero acceleration to mimic Richtmyer-Meshkov instability where mixing occurs without external forcing [29]. The structural changes in the mixing layer were remarkably small, and the turbulent mixing appeared to be frozen during the period of zero acceleration. Upon reacceleration, the RTI mixing layer quickly resumed development and did not exhibit any changes due to the intermission.

In this paper, we will explore the characteristics of statically stable flows evolving from a previously unstable turbulent mixing layer. We present a sequence of simulation campaigns examining both single and double-acceleration reversals. The first test campaign covers the single-reversal problem that is called the accel-decel (AD) case, in which the instability grows under a constant acceleration until the time (t_1), followed by a deceleration of indefinite duration. This time instant (t_1) is chosen such that the constant-acceleration RTI mixing layer has reached its self-similar behavior [4] that also allows to generate internal waves during the deceleration period. For the second test campaign, we conducted a series of simulations with double reversals, the accel-decel-accel (ADA) cases. For all the ADA simulations, the first reversal instant is kept constant at time t_1 ; the deceleration period is varied prior to reacceleration after a time t_2 . To permit comparison after the reacceleration we also performed a constant-acceleration RTI case which is referred to as the CG case. Our previous work [27] has shown evidence of internal waves in the mixing layer during the deceleration period ($t_1 < t < t_2$) that results in oscillatory behavior in the anisotropy and mass-flux tensors. Here, we study this internal wave oscillatory behavior in considerably more detail. We hypothesize that varying the duration of deceleration ($t_2 - t_1$) allows the internal waves to redistribute energy in the mixing layer between kinetic and potential energy; the choice of t_2 thus affects the properties of subsequent RTI growth after reacceleration. Depending on the phase of these oscillations, at the moment of acceleration reversal (t_2), subsequent growth evolves from substantially different initial conditions. The AD test campaign can be considered as a special case where $t_2 \rightarrow \infty$ and informs us of the long-term behavior of statically stable mixing initialized in this way. We find it useful to study this case to confirm the persistence of behavior over many cycles. While this case was motivated by academic concerns, there are many instances in atmospheric, oceanic, and astrophysical contexts where decaying turbulent layers form in a density-stratified flow. We choose Atwood numbers to explore density differences that are non-Boussinesq ($A = 0.5$) to allow comparison with previous studies [24,25,27–30].

II. METHODS

The governing equations used in this study are the incompressible Euler equations together with the implicit large-eddy

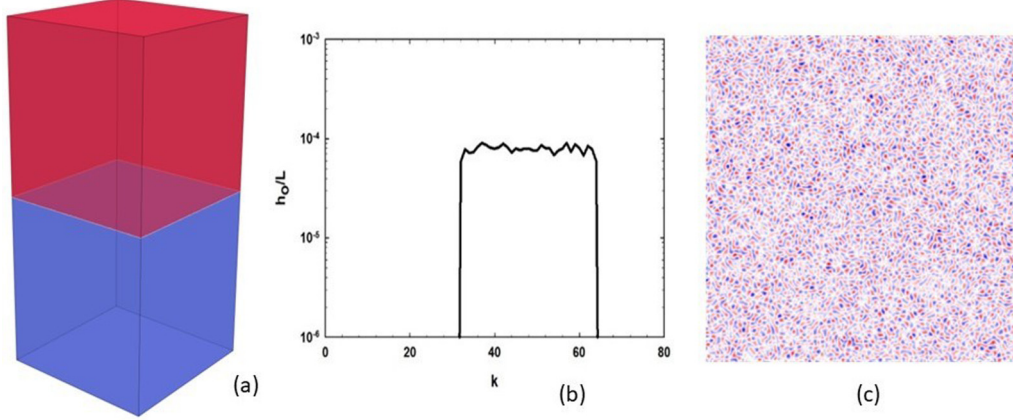


FIG. 1. (a) Schematic of the computational domain showing the heavy (red) and light (blue) fluids and their interface at $z = 0$, (b) azimuthally averaged initial perturbations with energy in the modes 32–64, and (c) initial perturbations in physical space at $z = 0$.

simulation technique that is explained below. The equations include

$$\text{Volume conservation : } \nabla \cdot \vec{v} = 0; \quad (2)$$

$$\text{Scalar transport : } \frac{Df}{Dt} = 0; \quad (3)$$

$$\text{Momentum : } \frac{D(\rho\vec{v})}{Dt} = -\nabla p + \rho\vec{g}, \quad (4)$$

where \vec{v} is the velocity vector, $\vec{v} = (u, v, w)$, ρ is the density, p is the pressure, $\vec{g} = (0, 0, g_z)$ is the gravity field, and D/Dt refers to the material derivative. In addition, f represents the nondimensional density, or mixing fraction, defined as $f = (\rho - \rho_H)/(\rho_L - \rho_H)$. Here, ρ_L and ρ_H represent the light and heavy fluids densities, respectively. In this study, the primes represent the Reynolds fluctuation of a field and the angle brackets $\langle \cdot \rangle$ represent the averaged over horizontal plane at the initial flow interface.

A. Problem setup and initial conditions

In this study, we use a three-dimensional computational domain with dimensions $L \times L \times 3L$ in the x , y , and z directions (where $L = 1.0$ cm). A grid resolution of $256 \times 256 \times 768$ was used for all calculations. The initial interface of the two fluids was set at $z = 0$ with the heavier fluid bounded between the interface and the top boundary of the domain at $z = 1.5$ cm and the lighter fluid contained between the interface and the bottom boundary of the domain at $z = -1.5$ cm [see Fig. 1(a)]. The boundary conditions are periodic in the x - and y directions and are zero-flux conditions at the top and bottom surfaces of the domain (z direction). An acceleration field of magnitude $g_z = 4.00$ cm/s² was applied since this corresponds well with existing literature [25,27]. For our $A = 0.5$ simulations, the densities of the fluids were selected as $\rho_L = 1.00$ g/cm³ and $\rho_H = 3.00$ g/cm³. The densities of the fluids were selected as $\rho_L = 1.00$ g/cm³ and $\rho_H = 1.05263$ g/cm³ for the $A = 0.05$ case. All simulations were initialized with the same interface perturbation function

[12,33,34]:

$$h(x, y) = \sum_{k_x, k_y} a_k \cos(k_x x) \cos(k_y y) + b_k \cos(k_x x) \sin(k_y y) + c_k \sin(k_x x) \cos(k_y y) + d_k \sin(k_x x) \sin(k_y y) \quad (5)$$

where a_k , b_k , c_k , and d_k are randomly chosen Fourier amplitude coefficients within a narrow band of wave number ($k = \sqrt{k_x^2 + k_y^2}$): modes 32–64, following the approach in the α -group study [34]. The amplitude coefficients are scaled to produce the desired rms amplitude of $3.15 \times 10^{-4} L$, where the energy-density spectrum is calculated according to [33]

$$\frac{\langle h_0'^2 \rangle}{2} = \int_{k_{\min}}^{k_{\max}} E_{h0}(k) dk. \quad (6)$$

The spectrum, together with a contour plot of the ICs, can be seen in Figs. 1(b) and 1(c). The diffused interface is calculated according to an error function that blends mass fraction, c , across the interface: $c = [1 + \text{erf}(10^4 z)]/2$. The selection of a narrow-band IC spectrum at high wave numbers was made to permit close comparison with previous studies [24,33,34]. Over time, due to nonlinear mode coupling, energy at high wave numbers will migrate towards the low wave-number end of the spectrum, allowing it to reach self-similarity [25,27,33–35].

B. Acceleration profiles and length scales

Previous studies [25–27] of variable acceleration RTI have used a Heaviside step function to generate the acceleration profiles:

$$g_z = g_0[-1 + H(t - t_1)(2) - H(t - t_2)(2)]. \quad (7)$$

In those studies, the duration of the first acceleration and the subsequent deceleration times were equal, with the focus on flow evolution in response to the reversals. The chosen acceleration profile begins with $g_0 = 4$ cm/s² for $t < t_1$; both H step functions are zero. Upon reaching t_1 , the acceleration reverses direction, and the two-fluid system switches from an RTI unstable configuration to a stable configuration. After the second acceleration reversal, the system returns to the RTI

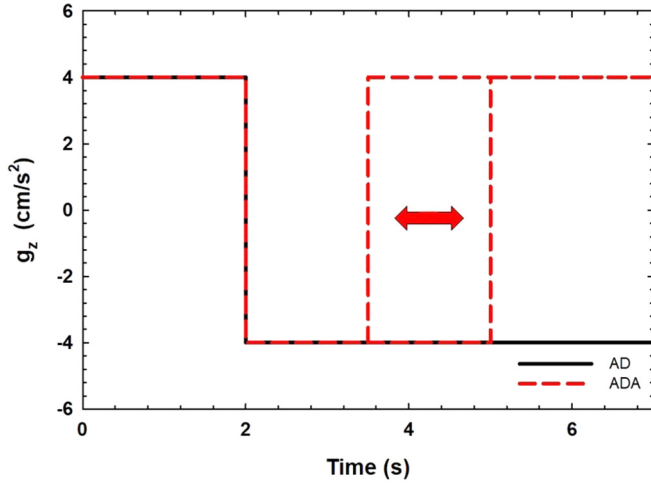


FIG. 2. Representative *accel-decel* and *accel-decel-accel* profiles used for the current study. For the ADA simulations, the deceleration time is varied, as indicated in the figure.

unstable configuration for all times $t > t_2$. A representative ADA profile is presented in Fig. 2 with t_1 and t_2 chosen as 2 and 4 s, respectively, for illustration similar to prior studies [25,27]. In this paper, we focus mainly on the effects of (a) an indefinite deceleration period (AD), $[t_2 - t_1] \rightarrow \infty$; and (b) a variable but finite deceleration period (ADA) $[t_2 - t_1]$; t_1 was kept constant while (t_2) was varied. In previous studies, a length scale $Z(t)$ was introduced as an acceleration-independent measure of mixing-layer progress [25,27,36] and works well for cases where the imposed acceleration field does not change sign. This length scaling cannot meaningfully be applied in the present work because $Z(t)$ passes through zero when the duration of acceleration and deceleration are equal, but our evidence indicates that the mixing layer never returns to zero thickness. Instead, to accommodate for variable periods of t_2 , we redefine the length scale $Z_{\text{ADA}}(t)$ shifted in time origin as

$$Z_{\text{ADA}}(t) = Ag_0(t - t_2)^2 \quad (8)$$

This definition ensures that during reacceleration, $Z_{\text{ADA}}(t)$ grows from t_2 at the same rate as the constant acceleration RTI and allows for comparison between the two cases.

C. Computational details

All simulations were performed using MOBILE, a massively parallel, three-dimensional variable-density, finite-volume incompressible flow solver that uses an ILES technique. MOBILE has been validated for fluid mixing, and transport problems, including single-mode and multimode RTI flows up to $A = 0.9$ [25,27,37–39], Kelvin-Helmholtz instability [40], and systems with variable acceleration [41]. Mass and momentum are conserved subject to an incompressibility constraint, and a fractional step approach is employed, decoupling hyperbolic (advective transport), parabolic (viscous dissipation, and scalar diffusion), and elliptic (pressure-velocity correction) components. It performs a sequence of total-variation bounded one-dimensional advective

subproblems, similar to Youngs [3] and Andrews [42], to eliminate unphysical oscillations around steep material gradients and in order to maintain numerical stability for the full three-dimensional problem, even when the gradients only marginally satisfy the Nyquist limit based on the mesh resolution. Additional computational details can be found in Ref. [40].

D. Dynamic mode decomposition analysis

In our previous work [27], the oscillatory behavior during the deceleration period of an ADA configuration was observed and attributed to internal wave activity. Here, we analyze the internal wave by introducing a linear algebraic tool to quantify the oscillatory features by decomposing them into linear modes by using the dynamic mode decomposition (DMD) technique [43]. Closely related to proper orthogonal decomposition, DMD takes an observable representation of the system's state, expressed as a vector y^k of length n at some time ($k\Delta t$), and finds the best-fit system evolution operator, A , that satisfies a discrete linear update, $y^{k+1} = Ay^k$, over an averaging period. If a matrix Y is composed of a temporal sequence of column vectors (of states y^1, \dots, y^{m-1}) and Y^+ represents the shifted-by-one sequence (y^2, \dots, y^m) then, $Y^+ = AY$. Suppose we let $Y = U \Sigma V^T$ where Σ is a diagonal matrix of singular values by convention ordered to be decreasing, columns of U form the corresponding left singular vectors of Y , and the right singular vectors of Y appear in rows of V^T ; then we find a great deal of information redundancy in the sequence. Locally, flows tend to be both spatially and temporally coherent, and so this reduces the linear independence of one state vector with respect to another, and the evolution operator is typically sparse and singular. This redundancy is exploited to reduce the dimensionality of the evolution operator from $n \times n$ to retain contributions from only the most significant p modes. We denote \hat{U} as the p truncation of the full matrix U . An approximate principal-axis transformation $A \approx \hat{U} \hat{A} \hat{U}^T$ into the truncated basis \hat{U} yields a dense, well-conditioned $p \times p$ reduction, given by $\hat{A} = \hat{U}^T Y^+ V \Sigma^{-1}$, that closely approximates the dynamic properties of the original. A further eigendecomposition, $\hat{A} = \hat{R} \hat{\Lambda} \hat{R}^{-1}$, provides a complete diagonalization, $A \approx \hat{U} \hat{R} \hat{\Lambda} \hat{R}^{-1} \hat{U}^T$, and the pairings $\hat{U} \hat{R}$ are known as the dynamic modes. In general, they form in conjugate pairs, with the phase of each i th eigenvalue pair (λ) determining its frequency according to

$$\omega_i = \tan\left(\frac{|\text{Im}\lambda_i|}{|\text{Re}\lambda_i|}\right). \quad (9)$$

By performing a transformation with respect to the inverse dynamic modes, $z^k = \hat{R}^{-1} \hat{U}^T y^k$, one can evolve each transformed mode independently in time according to $z^{k+1} = \Lambda z^k$, then invert the transformations to reconstruct a continuous sequence of images.

III. RESULTS AND DISCUSSION

The results from our simulation campaigns are subdivided into two sections. In Sec. III A, the case of single-acceleration

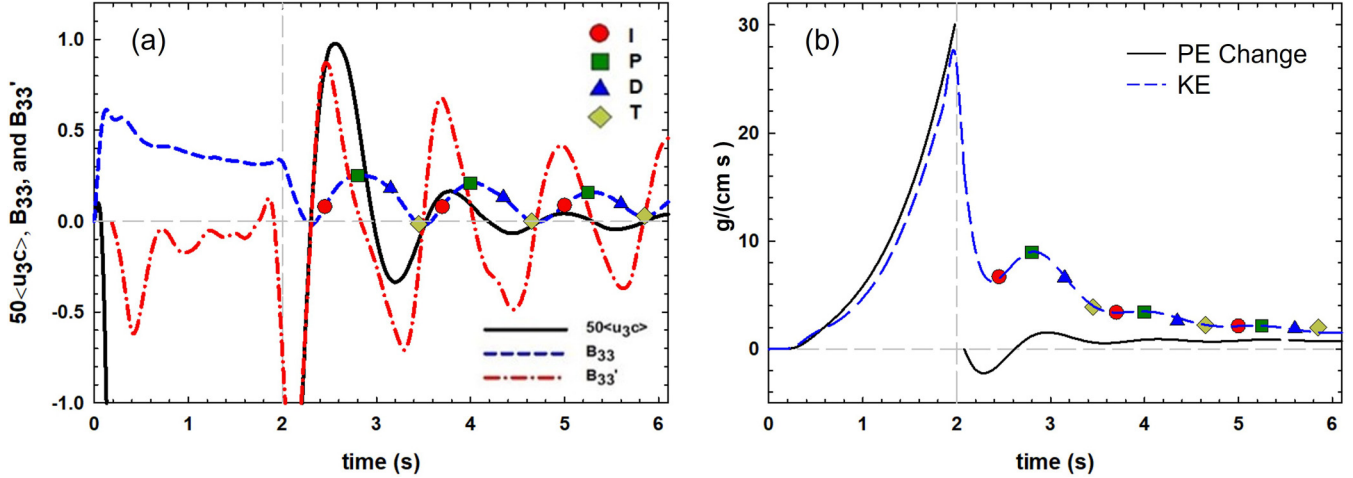


FIG. 3. (a) Oscillatory (internal wavelike) behavior observed in the vertical component of anisotropy tensor (B_{33}), its time derivative B'_{33} , and the mass flux $\langle u_3c \rangle$, and (b) time evolution of total KE and total change in PE during the deceleration period for an RTI mixing layer undergoing a single acceleration reversal (AD case). The acceleration reversal occurs at $t = 2$ s. The oscillations are used for selecting the reacceleration time, t_2 , for the ADA test cases (see Table I). Symbols denote the reacceleration times for I, P, D, and T cases.

reversal (AD) is discussed. Oscillatory behavior of mass flux and anisotropy tensor was observed, and a DMD technique is used to analyze the internal-wave behavior during the deceleration period. Section III B discusses the ADA simulation cases where the acceleration is reversed twice. The sensitivity of the duration of the deceleration period due to the internal wave dynamics on the reacceleration of the RTI mixing layer is quantified. The phase of the dominant oscillation at which acceleration is reversed for the second time is discussed. Finally, in Sec. III B 1, the evolution of second-order statistics during the period of re-acceleration is examined. We observe a strong sensitivity in the transient behavior of RTI after re-acceleration as an important consequence of the wave activity that arises during the deceleration period.

A. Dynamics of RTI under single-acceleration reversal

In the AD simulations, the interface is accelerated (unstable, $g_0 = -4$ cm/s²) until t_1 of 2 s ($time = 2$ s); beyond this, the interface is decelerated (stable, $g_0 = +4$ cm/s²). The deceleration period is extended until $t \sim 6.7$ s. This is sufficiently long to characterize the flow as the kinetic energy within the flow approaches to the value of zero. Shortly after the first acceleration reversal, the growth of the mixing layer ceases, which is consistent with the previous findings [25,27,29]. This indicates that the growth-rate parameter, α , introduced in Eq. (1), goes to zero during the deceleration period with minor fluctuations due to the internal wavelike motions within the mixing layer. The Reynolds stress anisotropy tensor \mathbf{B} is a quantity that emphasizes perturbations in mean turbulent kinetic energy away from isotropy by subtracting the expected value for an isotropic turbulent flow as [44]

$$B_{ij} = \frac{\langle u_i u_j \rangle}{\langle u_k u_k \rangle} - \frac{\delta_{ij}}{3} \quad (10)$$

where $i, j = 1, 2, \text{ or } 3$, corresponding to the x -, y -, and z axes, respectively. From the definition, the components of the anisotropy tensor where $i = j$ are bounded between values of $-1/3$ and $+2/3$; the total sum of all three components must equal to zero. Values of $-1/3$ correspond to zero energy ascribed to that component, whereas values of $2/3$ indicate all energy is located in that component. In a special isotropic flow case, the three diagonal components of the tensor, B_{11} , B_{22} , and B_{33} , must all equal zero. The classical RTI is known to be highly anisotropic in the acceleration direction ($B_{33} \neq 0$) and is horizontally isotropic ($B_{11} = B_{22}$) because the flow has symmetry in the horizontal direction [45,46]. In addition, the examination of B_{33} shows that it remains maximal at the center of the mixing layer [4,7,47]. The temporal evolution of the vertical component of the anisotropy tensor (B_{33}) is shown in Fig. 3 for density differences that are non-Boussinesq ($A = 0.5$). It was observed that the oscillation amplitude progressively decreases with the vertical velocity being highly anisotropic at relatively late times. Simulations were also conducted for the Boussinesq case ($A = 0.05$), and similar observations were observed irrespective of Atwood number and are not presented for brevity. To investigate the mechanism behind this behavior of B_{33} , we also plot the mass flux $\langle u_3c \rangle$, and the time derivative of the vertical component of the anisotropy tensor (B'_{33}) at the center plane ($z = 0$). The values of mass flux are multiplied by a constant value of 50 to aid in comparison with B'_{33} . In classical RTI [48], negative values of mass flux (having the same sign as the acceleration) represent energy conversion from potential energy (PE) to kinetic energy (KE); this conversion is global as the difference in PE in the pure fluids gets converted to KE in the RTI mixing layer [7,33]. For the AD case, there occurs a rapid increase in mass-flux value after the acceleration reversal at $time = 2$ s; since the mixing layer becomes statically stable beyond this point, there is no net transfer of energy from PE to KE. However, as observed in Fig. 3, the mass flux $\langle u_3c \rangle$ (where $c = f - (f)$), oscillates around a value of zero, indicating a persistent internal wave-induced energy exchange between PE

TABLE I. Nomenclature of RTI simulations reported in this paper: constant gravity (CG), accel-decel (AD), and accel-decel-accel (ADA). The ADA cases are further labeled as increasing (I), peak (P), decreasing (D), and trough (T) based on the vertical component (B_{33}) of the anisotropy tensor with values of the second reversal instant listed for different oscillatory periods of B_{33} .

Case nomenclature	Time (s)				
	First reversal	Second reversal			
Constant gravity (CG)	NA	NA			
Accel-decel (AD)		NA			
Accel-decel-accel (ADA)		Increasing (I)	Peak (P)	Decreasing (D)	Trough (T)
	1	2.45	2.80	3.15	3.45
ADA Period #	2	3.70	4.00	4.35	4.65
	3	5.00	5.25	5.60	5.85

and KE that is consistent with the oscillatory behavior of B_{33} during deceleration.

A comparison between the time derivative B'_{33} and mass flux in Fig. 3 provides further evidence that PE and KE energy exchange over one period of oscillation is responsible for the changes we observe in key turbulent statistics. A consistent offset in phase angle between B_{33} and mass flux of around $\pi/2$ is observed with peaks in mass flux correlated closely with peaks of B'_{33} . A high positive value of mass flux signifies a continued local transfer of PE to KE within the mixing layer. Any increase in KE arises from localized pockets of fluid that are relatively buoyant with respect to its surroundings, and such pockets will tend to move vertically more than horizontally, leading to a temporary increase in statistical anisotropy. The return phase coincides with the mass flux reaching a negative value signifying a high rate of transfer locally in the opposite direction from KE to PE, with the mixing layer becoming more isotropic. We classify the stationary and inflection points of B_{33} as peaks (P) where the flow is highly anisotropic and troughs (T) where it is almost isotropic; a region where anisotropy is increasing (I) between the troughs and peaks, and a region where anisotropy is decreasing (D) between the peaks and troughs (see Fig. 3). These four-phase references serve to classify, in our ADA campaign detailed in Sec. III B, our selected reacceleration times (t_2). For each oscillatory period of B_{33} , the reacceleration time (t_2) values were selected and denoted as increasing anisotropy (I), peak anisotropy (P), decreasing anisotropy (D), or trough anisotropy (T). A complete list of *time* values and their denotations for the subsequent ADA cases is listed in Table I. All points are chosen such that the *time* value accurately represented their respective segment of the B_{33} curve and represent a different balance and redistribution phase of the PE to KE transfer process. Figure 3(b) presents time evolution of total KE and total negative change in PE for the AD case. Hence, the positive value of change in PE represents discharge of the PE. As it is seen, at early time ($t < 1$ s) most of the PE is converted to the KE. This finding is confirmed consistent with the direct numerical simulations of the buoyancy-driven homogeneous variable-density turbulence [8]. The sign change in PE at time = 2 s is related with the PE gain just after the deceleration due to the flow inertia during the first acceleration period. The figure suggests a similar conclusion with Fig. 3(a). In subsection III B 2, we will proceed to show that in ADA cases, they are the principal predictors of RTI growth after reacceleration.

1. Internal wave dynamics during deceleration period

In this subsection, we focus on the dynamics of the internal waves during deceleration. The behaviors we observe have a slow dominant timescale compared with the turbulent motions established during the initial RT mixing-layer growth, so we consider the case of a single acceleration reversal *accel-decel* (AD) with prolonged deceleration to observe trends over several periods of wave oscillation. During the initial acceleration, potential energy present in the initial density stratification is incrementally converted into kinetic energy. By enabling molecular mixing, this kinetic energy facilitates the release of further potential energy, and the layer of mixed fluid grows in volume. One consequence of this mixing is that an initially sharp-density interface becomes progressively smoother and the mean-density gradient (typically measured as an average across the center plane) reduces accordingly. However, at the small scale, density gradients remain steep, especially near the outer boundary of the mixing layer, and this boundary is characterized by well-defined coherent structures penetrating above (bubble) and below (spike) the mixing layer, which act to release further potential energy to sustain the instability.

We observe that during deceleration, coherent structures previously extractive of potential energy now act to stabilize the system by doing work against the stratification. High-density gradients present at the instant of reversal become rapidly lower, using the supply of existing kinetic energy at the small scale to do mixing and thereby convert it back into potential. We find in Fig. 4(a) that the quantity of molecularly mixed fluid grows rapidly at this juncture. Without a mechanism to release ever-increasing potential energy, previously coherent structures collapse and lose their coherence, as may also be inferred from this figure. While the smallest scales exchange kinetic energy for potential most rapidly, there is a broad distribution of scales in the flow at the point of acceleration reversal, and the longest of those (associated with mean motions in the domain) are persistent because viscous and molecular diffusion act very slowly once density gradients reduce.

A useful rule of thumb to characterize the structural breakdown may be constructed by relating it to the overall stability of the stratified layer. We define a gradient Richardson number, Ri , here defined across the whole mixing layer to be $|N|/|S|$, where $S^2 = \langle du_x/dz \rangle^2 + \langle du_y/dz \rangle^2$, since other

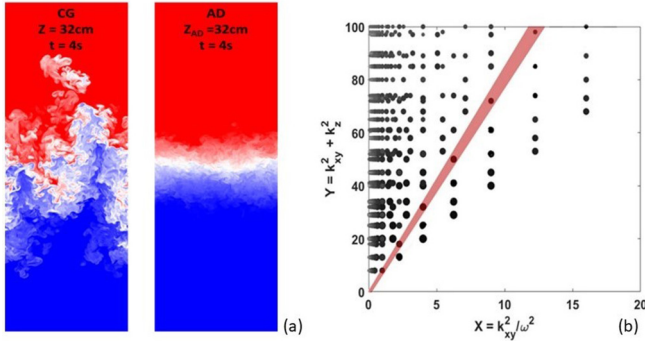


FIG. 4. (a) Vertical density contours for the CG and AD cases at $t = 4$ s, $Z = 32$ cm. (b) Kinetic energy is Fourier transformed and mapped onto transformed axes in which N^2 is a linear gradient. Points sampled in Fourier space are represented as black dots with radii that scale with the logarithm of energy. The red overlay is the region satisfying the dispersion relation for observed values of N and thus admits resonant internal wave activity.

contributions cancel in a horizontally periodic domain. We find that is found to be $Ri > 4$, at $t = 2$ s, indicating (since $Ri > 1$) a regime of stable wave motion, at the beginning of the deceleration period. The behavior of stable stratifications differs fundamentally from unstable stratifications. The simplest form of Taylor's model [2,39] for unbounded linear-exponential growth of an unstable density interface predicts an exponent “ n ” given by $Agk = n^2$, where A is the Atwood number, g is the strength of the acceleration field, and k is the wave number of a perturbation to the interface. When acceleration acts in the interface-destabilizing direction, the exponent n is real. Conversely, when it acts to stabilize the interface, n is complex, and produces oscillatory motion: traveling waves across the interface. The detail of any wavelike behavior is dependent on whether the mixing region, which has acquired appreciable thickness by the reversal time, oscillates as a diffuse interface between upper and lower layers, or as a region that as a whole is static but within which lies a continuous stratification that supports the oscillatory motion. Our statistical analysis indicates the latter. The type of wave motion supported in continuous stratifications is known as internal gravity waves [49].

The key question Fig. 4(b) seeks to resolve is whether the characteristics of RTI turbulence shortly after an acceleration reversal have a distribution of energetic wave numbers and frequencies that naturally satisfies the dispersion relation [Eq. (A2)]. We approach this question by overlaying the dispersion curve on the energy spectrum. It is convenient to do so in a transformed axis system. In a decelerating mixing region, we expect statistical homogeneity across a horizontal plane and differing spectral behavior aligned with the acceleration, so we choose to decompose wave-number space into a horizontally averaged mean, k_{xy}^2 (see the Appendix) whose values are constant on circles in the horizontal Fourier plane, and preserve k_z . Thus, we may write the dispersion relation in three dimensions in terms of the transformed variables, $X = \frac{k_{xy}^2}{\omega^2}$, obtained from a ratio of the horizontal wave number to temporal frequency, and $Y = k_{xy}^2 + k_z^2$, the squared magnitude of the wave number. It follows that Eq. (A2) may be written

as Eq. (A3) and so spectral features satisfying the dispersion relation will populate a straight line with gradient N^2 .

Working from the definition of the Brunt-Väisälä frequency [Eq. (A1)], the natural frequency of motion in a stably stratified fluid, we obtain the following bounds from the geometry of a Rayleigh-Taylor mixing layer at any stage of relaxation in terms of straightforwardly measurable variables:

$$\sqrt{\frac{2Ag}{h_b + h_s}} < N < \sqrt{\frac{-2g}{\rho_H + \rho_L} \frac{d\rho}{dz} \Big|_{\max}}, \quad (11)$$

which represents the range of admissible gradients of density across the RTI mixing layer. The red-shaded overlay in Fig. 4(b) indicates the admissible range of N^2 in which wave numbers and frequencies will satisfy the dispersion relation for resonant waves. Kinetic energy in the flow has been Fourier transformed and decomposed into horizontal and vertical directions and plotted in the transformed axes. The radius of the dots scales with the logarithm of kinetic energy at each sample point in Fourier space. As expected, many of the sampled points are associated with turbulent eddy activity and appear in the top left of the figure, where wave numbers are large and timescales are small. However, a substantial fraction of total energy is distributed across low wave numbers and long timescales. Several sampled points coincide with the dispersion curve, and this leads us to expect resonant wave activity during deceleration. Dispersion in this system is a key mechanism for the collapse of coherent structures as seen clearly occurring between the two contour panels in Fig. 4(a). A group velocity, $c_g = \frac{\partial\omega}{\partial k}$, which defines the rate of transport of wave packets and strongly wave-number dependent velocities that satisfy the dispersion relationship. Wave packets will disperse in physical space with a rapid breakdown of coherent structures. While the loss of coherence is predominantly a linear process, nonlinear mode interactions are prevalent in RT-unstable systems through small-scale mixing processes and, in particular during deceleration, there is a further available nonlinear mechanism driven by wave-wave triadic interactions. The breakdown of coherent structures is thus an irreversible process, and the structures do not reappear.

The DMD technique described in Sec. IID was applied to the deceleration period of our RTI AD dataset, where we anticipate that a component of the motion in the mixing layer will be periodic. The truncated distribution of eigenvalues $\hat{\Lambda}_{ii}$ (see Fig. 5) cluster around a unit circle on the complex plane, indicating that most modes are neither growing nor decaying. Those dynamic modes are identified with lines through the origin that correspond to the frequency of the mode. Selected dynamic modes from the full sequence $\hat{U}\hat{R}$, which share the dimensionality of the original center-plane density-field images, are plotted in Fig. 6. The images of the dynamic modes with corresponding temporal frequencies are computed using Eq. (9). The magnitude of the singular value of a mode is related to the statistical variance of its rate of change throughout the image sequence. This quantity is linked to the kinetic energy of a mode, but this is quite distinct from its total energy content. Some modes with large variance represent motions with a limited vertical variation or that are predominantly due to localized eddy turnover, and in configurations such as ours where potential energy is a significant fraction of the

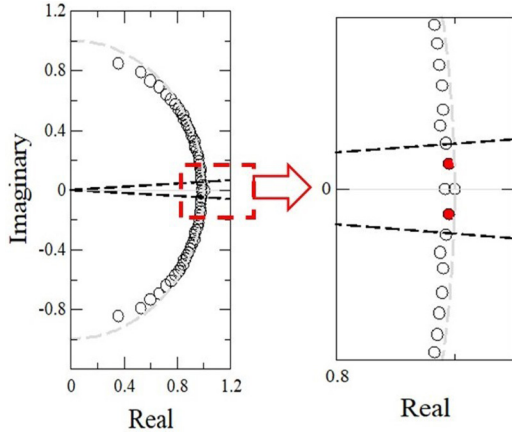


FIG. 5. DMD analysis of RTI AD case. The plot of the left side shows a truncated distribution of eigenvalues $\hat{\Lambda}_i$ and is plotted on a complex plane. The dashed gray line indicates a unit circle, and the dashed black lines indicate the buoyancy frequency. The zoomed subfigure on the right highlights the eigenvalues that correspond to the internal waves present during the RTI deceleration phase.

total [7,33], these are less influential than their variance may suggest.

The dynamic modes that appear earliest in the sequence are conjugate pairs of oscillatory modes representing eddy turnover activity and have broadly similar features to Fig. 6(a), which is the mode with the largest singular value. One may view this set of modes as a spectral decomposition of turbulence from the time- to the frequency domain, where the basis functions are found by a least-squares fit to the data rather than by projecting onto regularly spaced fixed-frequency Fourier modes. In Fig. 6(b), we obtain a mode at zero frequency, and this represents the background statically stable density stratification. This mode has no conjugate pair since it lies on the real axis in Fig. 5.

We now turn our attention to the resonating internal wave modes. We find two energetic modes identified by the DMD in Fig. 5 with frequencies that lie within or below the admissible range of N given in Eq. (11). An “effective” buoyancy frequency N is dependent on the sensitivity of the system to curvature in the density gradient throughout the mixing layer, but the range of uncertainty is small once the mixing layer is well developed. With some confidence we can identify the conjugate pair of modes indicated in Fig. 5 intersecting the black dashed line to correspond to vertically propagating critical internal waves. These “critical” waves oscillate vertically at the buoyancy frequency (N) of 2.53 rad/s, and have stationary phase. In a mixing layer these are identifiable as a standing-wave motion of the layer as a whole, and the shape of this dynamic mode is indicated in Fig. 6(c).

The frequency of the associated vertical motion corresponds exactly to oscillatory behavior found in the vertical component of the anisotropy tensor (B_{33}) and in the mass flux. The internal wave interpretation of vertical fluxes of mass and energy is therefore fully consistent with the picture laid out in Fig. 3. Given this corroboration, we infer that any modes with frequency below N must be propagating internal waves. In Fig. 5 we find one conjugate pair, indicated by the red

dots, and the corresponding dynamic mode shape is given in Fig. 6(d). As a visual guide, we overlay lines whose angle to the vertical is calculated using $\theta_i = \pm \cos^{-1}(\frac{\omega_i}{N})$, corresponding to the angle of propagation within the mixing layer. These waves may only propagate within the mixing layer where a density gradient exists. Towards the edges of the mixing layer the stratification weakens, and diagonally propagating wave packets will preserve their frequency but be refracted towards the vertical as N locally reduces. Our observations suggest that most wave energy remains within the layer, and therefore wave packets must reflect back from the edges.

Although propagating modes have now been shown to play an important role in the mixing-layer structure, not all internal wave motion manifests as waves propagating in specific directions. The spectrum of dynamic mode-associated turbulent scales all have $\omega > N$. We may also interpret such modes as internal waves, but these have “evanescent” form and radiate over short distances in all directions; there is no single direction of propagation, nor is there significant nonlocal transmission of wave packets. The reason for the change in behavior is that the governing equations for linear internal waves are hyperbolic when $\omega < N$ and so exhibit real-valued characteristics with a well-defined direction, but when $\omega > N$ these become imaginary, and the governing equations become elliptic. A thorough treatment of these issues is covered in work by Dobra *et al.* [50,51]. As already discussed, the rate of mixing is high during the deceleration period and this modifies the density stratification, and the buoyancy frequency will evolve as a consequence. A slow evolution of oscillation frequencies is to be expected, and this behavior may be seen clearly in Fig. 3.

B. Dynamics of RTI under two acceleration reversals (ADA)

After the second acceleration reversal, the mixing layer once again becomes RT unstable and starts to regrow. It has been shown in previous studies that RTI recovers to exhibit self-similar behavior on the long term, analogous to that observed in the constant-acceleration RTI [27]; the reacceleration might be considered as classical RTI initialized with a much thicker and more energetic interface between the pure fluids. Since our AD simulations demonstrate an oscillatory behavior prompted by PE to KE exchange due to internal waves reverberating within the mixing layer, the second acceleration reversal can be initiated at a time instant t_2 that corresponds to the phases I, P, D, and T corresponding to the oscillatory behavior of B_{33} discussed in Sec. III A. It is expected that RTI growth in the short term after t_2 depends strongly on the duration of the deceleration period. This short-term behavior may be key in some application areas, notably with ICF capsules, where the instability is not anticipated to persist long enough to recover the asymptotic self-similar behavior. Figure 7 shows clear qualitative differences in integral mix width and mixing states within the mixing layer for I, P, D, and T phases, and we provide a constant-acceleration case for reference (denoted CG). Vertical (midplane) slices of density contours are plotted in the top row of Fig. 7, and horizontal (at the height of the original interface) slices on the bottom row. These qualitative observations will now be

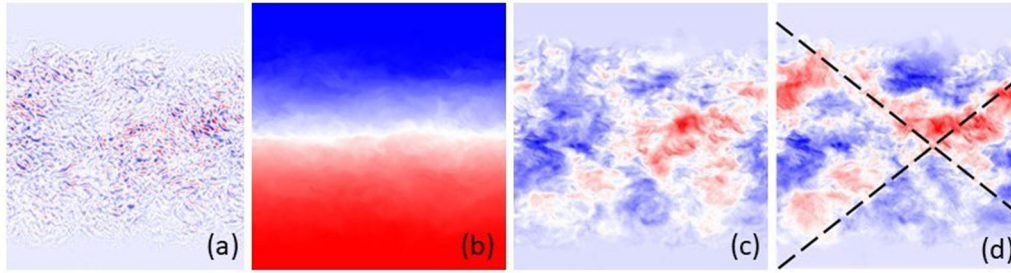


FIG. 6. Visualization of modes: (a) a turbulent mode, (b) the zero-frequency mode, (c) the critical B33 mode, and (d) a propagating internal wave mode. The dashed lines on the internal wave mode correspond to the direction of propagation implied by its frequency given in Fig. 3.

quantified in some detail by presenting key statistics of mixing layer width and second-order moments.

Figure 8(a) presents the integral mix width [Eq. (A4)], plotted as a function of time (s) for all cases with $A = 0.5$ investigated in this paper. The integral mix width for the different I, P, D, and T cases indicates a significant difference in the growth rate upon reacceleration. Since the 12 ADA cases each commence reacceleration at a different value of t_2 , an unmodified scaling on the basis of Z does not allow for direct comparison. As introduced in Eq. (6), we modify the scaling by shifting its time origin to t_2 , thus avoiding physically inconsistent outcomes, such as negative values. Once self-similar length scales are adjusted to account for the variation in t_2 , a consistent pattern emerges between common choices of phase I, P, D, and T across several oscillations [compare Figs. 8(a)–8(c)]. We note that growth rates follow the pattern $|D| > |P| \sim |T| > |I|$ and our simulations suggest that although their short-term development may be substantially different, in the long-term, any I, P, T, or D choice within an oscillation period is likely to produce a similar long-term trajectory. This long-term behavior is similar to the

self-similar growth of the classic RTI, Eq (1), and the growth of the W tends to become linear with Z_{ADA} . This is another indication that after reacceleration the RTI flow recovers itself in the long run. T is consistently anomalous with intermediate growth rates $|D| > |T| > |P|$, and so long-term trajectories remain delayed with respect to the others. Figure 8(d) represents the averages of the integral mixing widths over the first three oscillations. As observed in Fig. 3, when anisotropy is increasing (I), the mass flux has local maxima indicating exchange from KE to PE. When we choose reversals at Is, it takes longer for RTI to establish upon reacceleration. Equally, when we choose reversals at Ds, the energy exchange is in the opposite direction, and motions of the light and heavy fluids are already preferentially aligned with the acceleration vector, and for this phase in a direction favorable for instability growth. When we choose reversals at Ps and Ts, there is no significant directional preference within the flow as the mass flux is zero. The growth rate of the mixing layer for both D and I cases thus lies between the growth rates for the P and T cases. Further analysis of mixing-layer growth, decomposing the integral measure of its size into h_b and h_s , to identify any

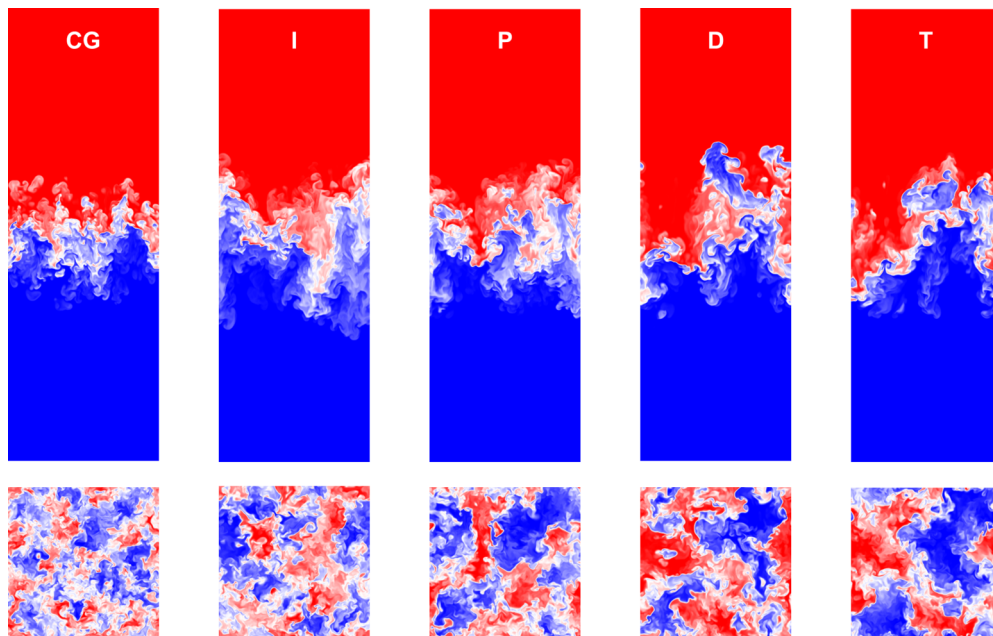


FIG. 7. Vertical and horizontal density contours for the CG at $Z = 12$ cm. I, P, D, and T cases are shown for $Z + Z_{ADA} = 12$ cm. The deceleration period is subtracted for I, P, D, and T cases to evaluate RTI mix states at similar values of $Z + Z_{ADA}$. The horizontal slices are taken from the height of the original heavy-light fluids interface.

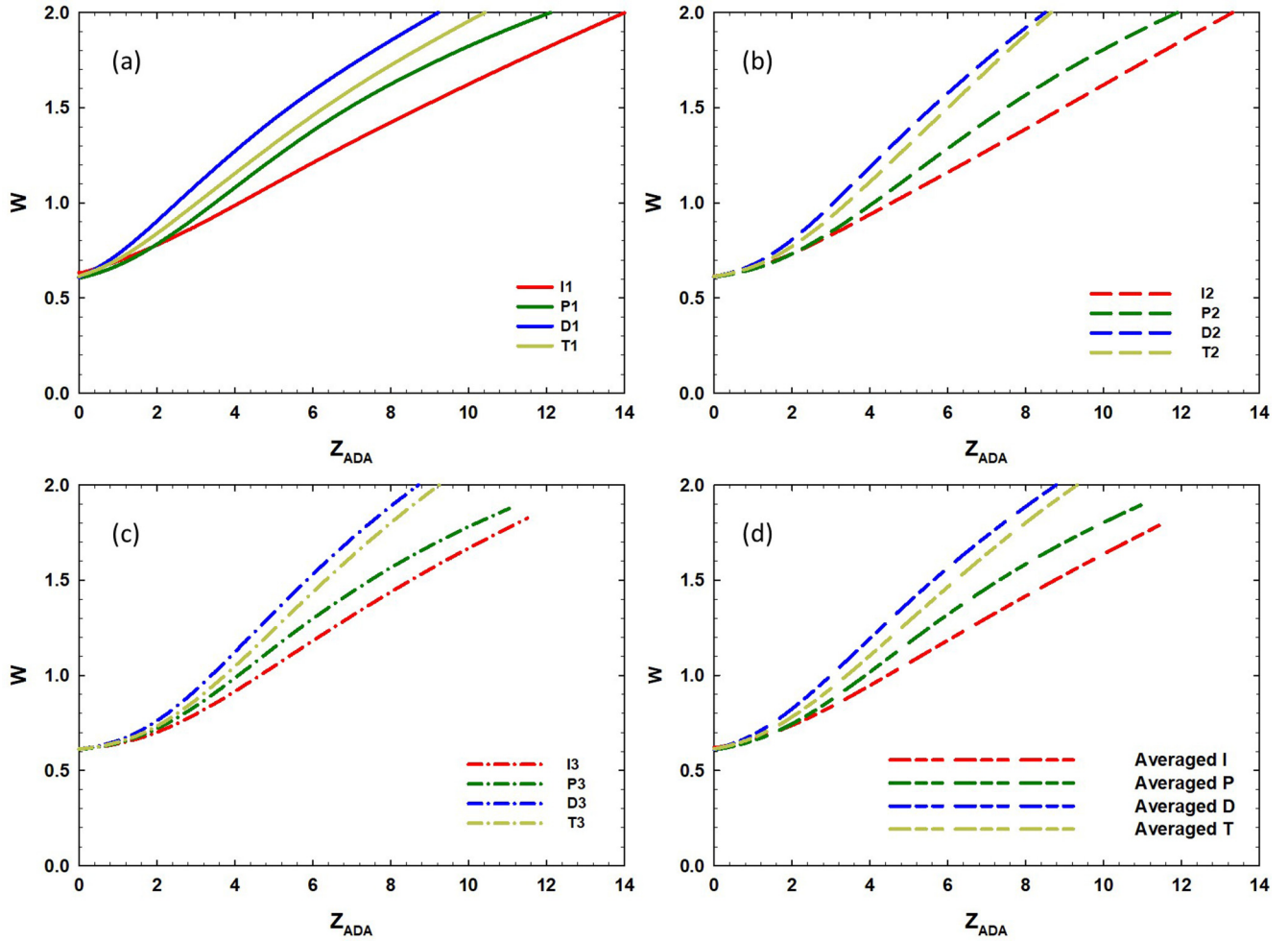


FIG. 8. The integral mixing width, W , scaled by Z_{ADA} for the (a) first-, (b) second-, and (c) third oscillatory period of B_{33} . (d) Average of integral mix widths over the three oscillatory periods during the RTI ADA reacceleration phase.

sensitivity to the I, P, D, and T phases is shown in Fig. 9. Bubble and spike widths (h_b and h_s) are estimated from the location where the plane-averaged values of the mole fractions of the light fluid reaches values of 99 and 1%, respectively,

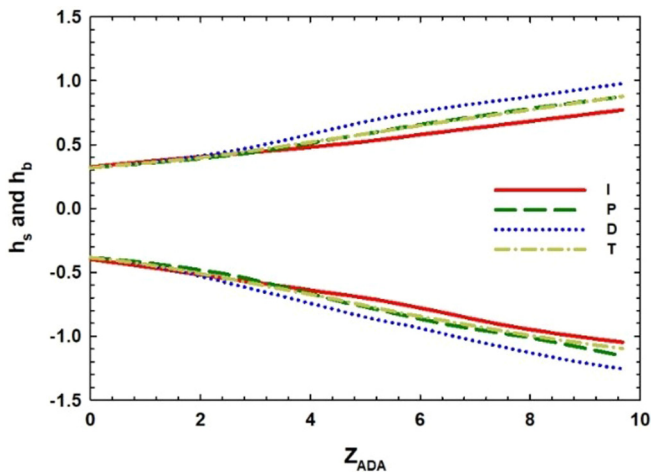


FIG. 9. Bubble and spike widths (h_b and h_s) averaged over the three oscillatory periods for ADA cases during reacceleration.

and averaged over three oscillations for phases corresponding to I, P, D, and T. The D and I cases exhibit, respectively, the fastest and slowest growth on average. As expected, the P and T cases are almost identical and occupy intermediate rates of growth. In addition, at large A , it has been reported that the growth rates of h_b and h_s are diverging as spikes grows faster than the bubbles [5]. This observation extends after the second acceleration as well and the h_b/h_s ratio stays approximately constant around the value of 0.8. Though our simulations extend over three full cycles of oscillation, total KE in the mixing layer significantly decreases with each subsequent oscillation of B_{33} , and we may therefore expect that the growth rate after reacceleration will become *progressively less sensitive to the phase*.

1. Evolution of the second-order moments for RTI under ADA

Second-order quantities obtained from moment equations have been reported to remain constant in the self-similar regime of classical RTI growth by Ristorcelli and Clark [4]. We seek to determine if the RTI ADA conforms to this expectation after the second acceleration reversal. The scalar variance $\langle cc \rangle$, the normalized mass flux, $\langle u_3 c \rangle / h_{\text{tot}}^{0.5}$, and the normalized vertical-velocity fluctuation $\langle u_3 u_3 \rangle / h_{\text{tot}}$, where

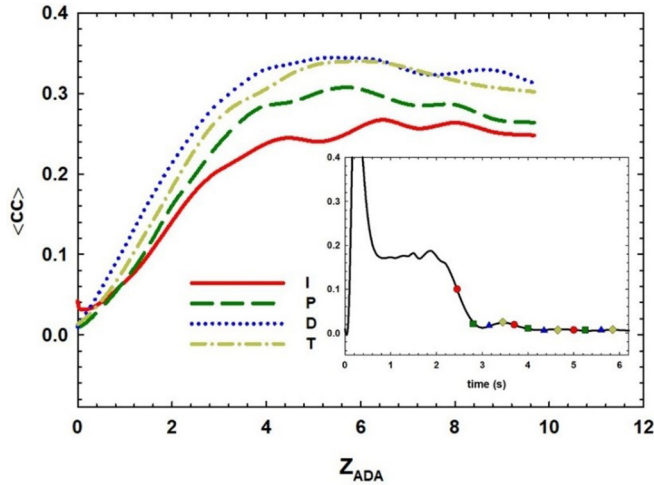


FIG. 10. Scalar variance $\langle cc \rangle$, averaged for each D, P, I, and T case over the three oscillatory regions. The inset plot shows the scalar variance of the AD case with reacceleration times marked.

$h_{\text{tot}} = h_b + h_s$, were determined taking planar averages at the initial interface location ($z = 0$) [4]. Similar normalization factors were also used by the authors in their previous study [23]. The scalar variance $\langle cc \rangle$ (where $c = f - \langle f \rangle$), the normalized mass flux $\langle u_3 c \rangle / h_{\text{tot}}^{0.5}$, and the normalized vertical-velocity fluctuation $\langle u_3 u_3 \rangle / h_{\text{tot}}$, were determined taking planar averages at the initial interface location ($z = 0$) [4]. In both cases of single (AD) and double (ADA) acceleration reversal, all three parameters drop to near-zero values and exhibit slight oscillatory behavior during the deceleration period of AD and ADA cases similar to the observations reported in Ref. [27]. During reacceleration, the scalar variance and normalized mass flux both return towards values comparable with those obtained during the initial acceleration. However, they exhibit sensitivity to the time instant (t_2) of second acceleration reversal and tend towards a constant value at late time.

The scalar variance $\langle cc \rangle$ is plotted in the inset to Fig. 10 for the AD case; the scalar variance is near zero for $t > 3$ s. Low values of the scalar variance correspond with greater molecular mixing [27], and the flow becomes well mixed at the center of the mixing layer, as seen earlier in Fig. 4(a). During reacceleration, the increasing anisotropy (I) cases exhibit the greatest mixing, whereas the decreasing anisotropy (D) cases exhibit the least, consistent once again with evidence from plots of the integral mix widths and field-slice data: faster growth is associated with a mixing layer that is less mixed [see also Fig. 7(d)]. Similar trends are observed for the mass flux $\langle u_3 c \rangle$ at the center plane. For $t > 3$ s, the mass flux oscillates with a small amplitude around zero. As shown in Fig. 11, after reacceleration, the mass flux returns to asymptotic (negative) values, suggesting a self-similar behavior. The transient behavior, however, is dependent on the choice of phase I, P, D, and T, and we note that a range of durations tends to reach a self-similar state. We anticipate that if the Ps and Ts are run longer, they will reach the self-similar value. Larger values of mass flux and scalar variance are associated with fast-growing mixing layers since they need to convert PE to KE at a more rapid rate.

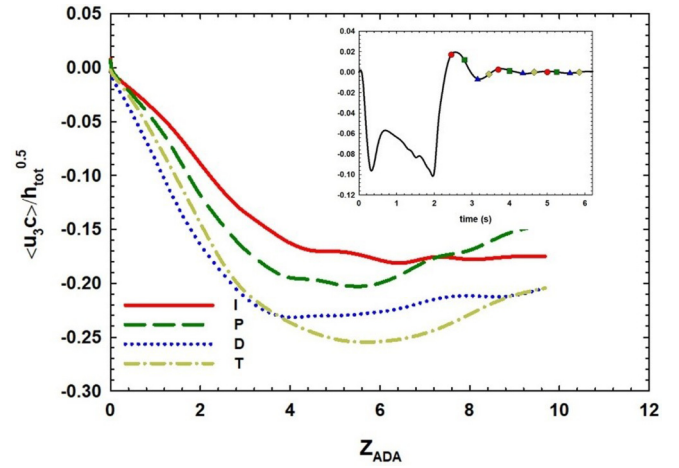


FIG. 11. The normalized mass flux $\langle u_3 c \rangle / h_{\text{tot}}^{0.5}$, averaged for each D, P, I, and T case over the three oscillatory regions. The inset plot shows the mass flux of the AD case with reacceleration times marked.

The vertical contribution to kinetic energy $\langle u_3 u_3 \rangle$, at the center plane is shown in Fig. 12. The results are consistent with our observations for the scalar variance and mass flux for the AD campaign. The vertical component of the kinetic energy is negligible for $t > 3$ s as oscillation amplitudes decay away. While our findings are critical to understanding the transient regimes during deceleration and reacceleration, the dynamics of the long-term is somewhat simpler, and we expect much less sensitivity due to the oscillation phase. It is also important to note that the PE rapidly releases, and KE increases similar to the classic RTI problem. The reacceleration stage follows a similar pattern as shown in the first acceleration stage in Fig. 3(b). We observed a small variation in reacceleration behavior when t_2 is chosen during the first oscillation period. In particular, we find for reversals at phases D and T, $\langle cc \rangle$ and $\langle u_3 c \rangle$ appear to reach self-similarity somewhat earlier. We believe that large structures from the

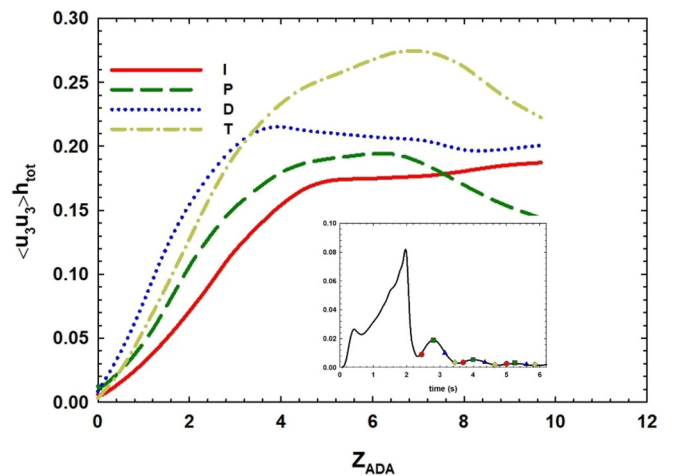


FIG. 12. The normalized vertical velocity fluctuation $\langle u_3 u_3 \rangle / h_{\text{tot}}$, averaged for each D, P, I, and T case over the three oscillatory regions for $A = 0.5$. The inset plot shows marked reacceleration times during the AD case.

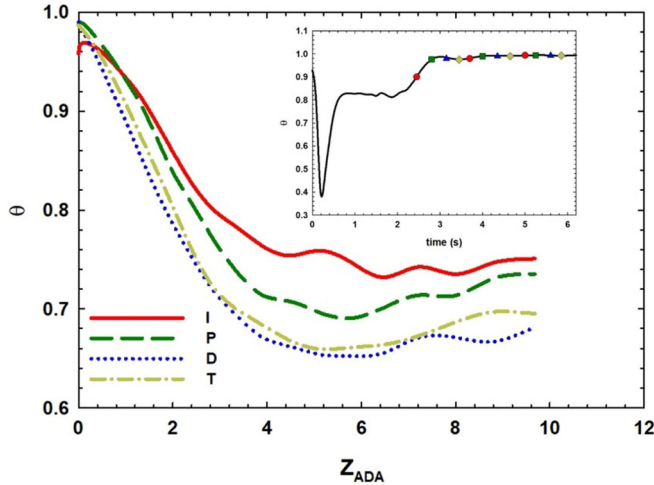


FIG. 13. θ averaged for each D, P, I, and T case over the three oscillatory regions. The inset shows the marked reacceleration times for the AD case.

initial acceleration may not yet have broken down so early in the deceleration period; thus, the onward evolution is directly influenced, and the patterns that arise from the phase may be less clearly visible if taken in isolation.

The molecular-mixing parameter θ , $\theta = \frac{(f(1-f))}{(f)/(1-f)}$, which exhibits similar patterns to the mass flux and scalar variance, is plotted in Fig. 13. We measure this value at the center plane ($z = 0$). The value of unity for θ signifies a fully mixed flow, and lower values imply a flow state that is less well mixed. In classical RTI, θ asymptotes to a value of $\theta \sim 0.8$. Here, for the ADA cases, although this asymptotic value is reached in the initial acceleration, in the AD campaign, we observe high levels of mixing during deceleration with asymptotic values of $\theta = 1$ at the center plane. At the subsequent reversal, these values again drop as the mixing layer during growth is consistently less well mixed. The fastest-growing example, D, generally has a sharper decrease to a lower value of θ . Conversely, the slowest-growing example, I, only slowly reduces to the expected asymptotic value of $\theta \sim 0.8$ and constitutes the upper bound for the presented cases (see Fig. 7 for qualitative mixing-state differences).

IV. CONCLUSIONS

In this study, we explored the behavior of RTI mixing layers under accel-decel (AD) and accel-decel-accel (ADA) acceleration profiles through a sequence of simulation campaigns. The application of deceleration to a previously Rayleigh-Taylor unstable system causes an oscillatory pattern to emerge in the anisotropy tensor and density-velocity correlations. The behavior of second-order moments that include scalar variance, mass flux, and kinetic energy converge for $t > 3$ s. Examination of the full spatiotemporal spectrum demonstrates the consistency of the oscillatory behavior with the resonance conditions for internal gravity waves within the mixing layer. The idealized internal wave equations were applied to the non-Boussinesq case ($A = 0.5$), even though they were originally derived for a Boussinesq case; in this study, internal wave behavior was observed for both cases. Second-order moments were also insensitive to Atwood num-

ber during deceleration. In the ADA campaign, we explored the sensitivity of reacceleration time on subsequent RTI growth and found that phase of the internal oscillation was the most reliable predictor. The mechanism underlying this dependency on phase was associated with the proportion of kinetic energy aligned with the vertical at the acceleration reversal.

Figure 14 illustrates the dynamics of the flow during the deceleration period. The I (increasing anisotropy) cases are representative of when the mass flux (u_3c) opposes the direction of reacceleration, as small structures have formed and travel quickly in the direction of deceleration. This leads to relatively slow growth because the mass flux must change direction before starting to globally convert PE to KE. Meanwhile, the D (decreasing in anisotropy) cases occur when the mass flux is maximally negative, so during reacceleration, it does not need to change sign before converting PE to KE. Thus, these cases grow fastest. The regrowth rates of the P and T cases lie in between I and D cases because the mass flux is neutral at these phases. Cases reaccelerated when kinetic energy is being most rapidly converted to potential grow up to 35% faster than those when the energy exchange is reversed. Reported second-order moments asymptote towards constant values, supporting the conclusion that self-similar behavior persists at late time similar to the constant-gravity case and is independent of the phase at which reacceleration was imposed. However, their short-term transient behavior, which is of primary interest, is highly sensitive to the duration of the deceleration stage and the phase of B_{33} behavior. The main conclusions of this study are as follows:

- (1) The first acceleration reversal leads to a stable stratification and an immediate cease in the growth of the RTI mixing layer. Hence, the self-similar growth-rate parameter, α , goes to zero during the deceleration stage.
- (2) After the second acceleration reversal, the response of the RTI flow strongly depends on the undergoing physics during the deceleration stage, such as it depends on the residual energy's distribution between the PE and KE.
- (3) To predict the regrowth of the RTI mixing layer due to reacceleration one should examine the internal wave dynamics that arises during the deceleration stage.
- (4) In the long term, the RTI ADA flow recovers its self-similar behavior for the first- and second-order parameters investigated in this study.

The data that support the findings of this study are available from the corresponding author upon reasonable request.

ACKNOWLEDGMENTS

A.B. would like to thank the U.S. National Science Foundation (Award No. 1453056) for financial support that made this work possible. The authors would also like to thank Zach Farley for participating in initial simulation campaign for this manuscript.

APPENDIX: CONDITIONS THAT PROMOTE INTERNAL WAVE MECHANISMS WITHIN RT MIXING LAYER UNDER DECELERATION

Linear internal gravity waves are a restricted solution of the Navier-Stokes equations in the case, where we

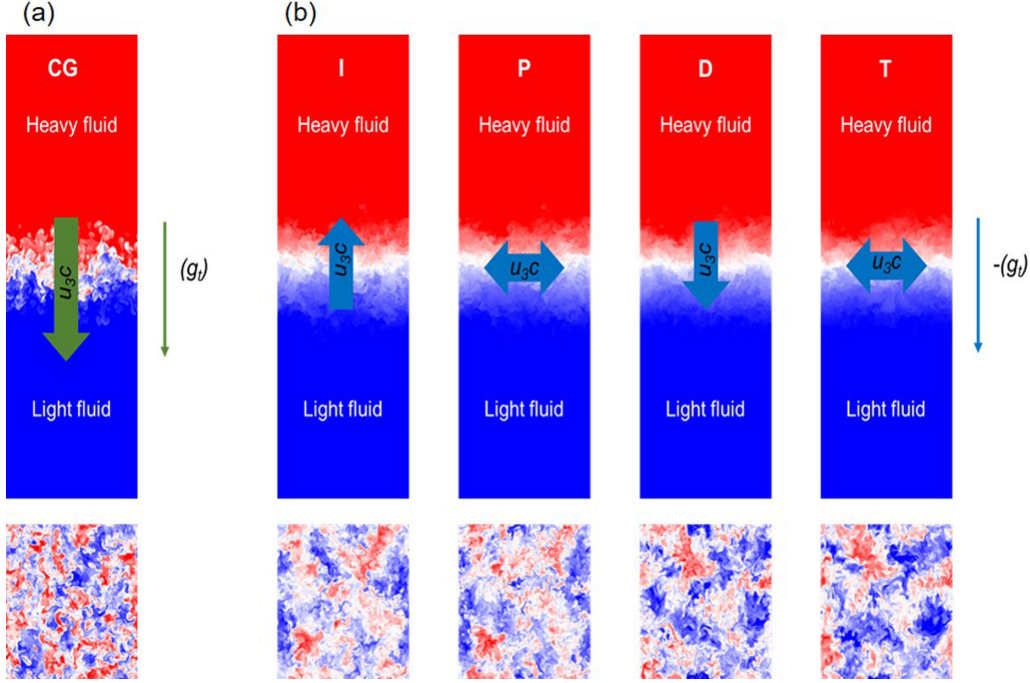


FIG. 14. Three-dimensional visualization of the density field where the behavior of the vertical mass flux $\langle u_3c \rangle$ during (a) classical RTI, and (b) RTI under deceleration at DPIT phases of the anisotropy tensor. As it is seen, in decreasing anisotropy (D) cases, mass flux behaves similarly to the classical RTI case, and the acceleration reversal at that point leads to the fastest regrowth. Meanwhile, the mass flux at the increasing anisotropy (I) point is just the opposite direction of the mass-flux behavior during the classical RTI; hence, these cases grow slowest. Besides, at anisotropy peaks (P) and trough (T) points, the behavior of the mass flux is almost neutral ($\langle u_3c \rangle \sim 0$), so their growth rates are between I and D cases. (Note that the horizontal slices are taken from the height of the original heavy-light fluids interface.)

assume inviscid flow and the nonlinear terms, which contain the advection operator $\mathbf{u} \cdot \nabla$, are considered negligible. The remaining derivative operators can be isolated into a complex-valued matrix \mathbf{P} that acts on a state vector ϕ , say, and the system arranged into a homogeneous form. Taking a single Fourier mode of ϕ , we can write $\phi = \hat{\phi} e^{i(\mathbf{k} \cdot \mathbf{x} - \omega t)}$, where for the simplest two-dimensional case, $\hat{\mathbf{k}} = [k_x \ k_z]^T$. The derivative operator \mathbf{P} then takes the complex-valued algebraic form $\hat{\mathbf{P}}$. For a homogeneous system, nontrivial symmetries are found when the determinant $|\hat{\mathbf{P}}| = 0$, and these correspond to resonant wave behaviors. From $|\hat{\mathbf{P}}| = \omega^2 - (-\frac{g}{\rho_0} \frac{d\rho}{dz}) \frac{k_x^2}{k^2} = 0$ arises a natural frequency,

$$N = \sqrt{-\frac{g}{\rho_0} \frac{d\rho}{dz}}, \quad (\text{A1})$$

known as the buoyancy (Brunt-Väisälä) frequency, and by examining the geometry of $k/\hat{\mathbf{k}}$ we may write the dispersion relation as

$$\omega^2 = N^2 \frac{k_x^2}{k_x^2 + k_z^2} = N^2 \cos^2 \theta, \quad (\text{A2})$$

where θ is the angle between the wave vector $\hat{\mathbf{k}}$ and the horizontal. Further examination of the properties of the determinant shows that waves travel through a density-stratified medium in beams perpendicular to $\hat{\mathbf{k}}$. It follows from the properties of an inverse cosine that these resonant conditions for internal waves only occur when $\omega < N$. In the case of an energetic stratified flow with a high Reynolds number, wave

beams may not be as easily observable as they are in the laminar conditions analyzed above. However, a statistical analysis can confirm their presence. In loose terms, one may associate certain frequencies ω with eddy turnover in a turbulent flow and wave number k with their length scale. Thus, we infer that only certain combinations of frequency and scale will give rise to a resonant wave condition.

In a decelerated mixing region, we expect statistical homogeneity across a horizontal plane and differing spectral behavior aligned with the acceleration, so we choose to decompose wave-number space into a horizontally averaged mean, $k_{xy}^2 = k_x^2 + k_y^2$, whose values are constant on circles in the horizontal Fourier plane, and preserve k_z . Thus, we may write the dispersion relation as $\omega^2 = N^2 \frac{k_{xy}^2}{k_{xy}^2 + k_z^2}$. We may express this in terms of substitute variables: $X = \frac{k_{xy}^2}{\omega^2}$ a ratio of the horizontal wave number to temporal frequency, $Y = k_{xy}^2 + k_z^2$, is the squared magnitude of the wave number, and it follows that

$$Y = N^2 X, \quad (\text{A3})$$

so spectral features satisfying the dispersion relation will populate a straight line with gradient N^2 . We seek to relate the conditions for internal wave resonance to those produced by a developing instability. By inspection, (11) may be written in terms of mean quantities defined for the mixing region as

$$N^2 = \frac{2Ag}{W}, \quad (\text{A4})$$

where A is the Atwood number, $W(t) = 6 \int \langle f_l \rangle \langle f_h \rangle dz$ is the horizontally averaged thickness of the region (integral mix width). Combining (A2) and (A3) and rearranging, we obtain

$$W(k_{xy}, k_z, \omega) = 2A \frac{X(k_{xy}, \omega)}{Y(k_{xy}, k_z)}. \quad (\text{A5})$$

The value of W can be measured from the turbulent scalar or velocity field during the accelerated instability over a range of locations in the Fourier space. Although the duration over which the flow may be deemed statistically steady is short, the resolvable range of ω includes frequencies associated with eddy turnover. We calculate W fields over

short-duration windows several times t during the accelerated instability. For each such flow state and any available coordinate triplet of $\{k_{xy}, k_z, \omega\}$, W predicts a mixing-region height consistent with the emergence of resonant internal waves if deceleration were to commence. A subset of these available coordinates satisfies the dispersion relation given in Eq. (A4), and one may look within this subset for values that match the current mean W . When such a match (in this study at t_1) is found, the gravity could be switched from acceleration to deceleration, in the expectation that the stably stratified flow would proceed to generate internal waves.

-
- [1] L. Rayleigh, Investigation of the character of the equilibrium of an incompressible heavy fluid of variable density, *Proc. R. Soc. London* **s1-14**, 170 (1882).
- [2] G. I. Taylor, The instability of liquid surfaces when accelerated in a direction perpendicular to their planes I, *Proc. R. Soc. London, Ser. A* **201**, 192 (1950).
- [3] D. L. Youngs, Numerical simulation of turbulent mixing by Rayleigh-Taylor instability, *Physica D* **12**, 32 (1984).
- [4] J. R. Ristorcelli and T. T. Clark, Rayleigh-Taylor turbulence: Self-similar analysis and direct numerical simulations, *J. Fluid Mech.* **507**, 213 (2004).
- [5] A. Banerjee and M. J. Andrews, Statistically steady measurements of Rayleigh-Taylor mixing in a gas channel, *Phys. Fluids* **18**, 035107 (2006).
- [6] W. H. Cabot and A. W. Cook, Reynolds number effects on Rayleigh-Taylor instability with possible implications for type-Ia supernovae, *Nat. Phys.* **2**, 562 (2006).
- [7] A. Banerjee, W. N. Kraft, and M. J. Andrews, Detailed measurements of a Rayleigh-Taylor mixing layer from small to intermediate Atwood numbers, *J. Fluid Mech.* **659**, 129 (2010).
- [8] D. Aslangil, D. Livescu, and A. Banerjee, Effects of Atwood and Reynolds numbers on the evolution of buoyancy-driven homogeneous variable-density turbulence, *J. Fluid Mech.* **895**, A12 (2020).
- [9] D. Aslangil, D. Livescu, and A. Banerjee, Flow regimes in buoyancy-driven homogeneous variable-density turbulence, presented at the *iTi Conference on Turbulence*, Springer Proceedings in Physics, Vol. 226 (Springer, Cham, 2018), pp. 235–240.
- [10] D. Aslangil, D. Livescu, and A. Banerjee, Variable-density buoyancy-driven turbulence with asymmetric initial density distribution, *Physica D* **406**, 132444 (2020).
- [11] O. A. Molchanov, On the origin of low- and middle-latitude ionospheric turbulence, *Phys. Chem. Earth* **29**, 559 (2003).
- [12] A. Haley and A. Banerjee, Role of initial conditions in unstably stratified hydrogen-air mixing zones, *Int. J. Hydrogen Energy* **36**, 11174 (2011).
- [13] Y. Zhou, Rayleigh–Taylor and Richtmyer–Meshkov instability induced flow, turbulence, and mixing. II, *Phys. Rep.* **723-725**, 1 (2017).
- [14] Y. Zhou, Rayleigh–Taylor and Richtmyer–Meshkov instability induced flow, turbulence, and mixing. I, *Phys. Rep.* **720-722**, 1 (2017).
- [15] G. Boffetta and A. Mazzino, Incompressible Rayleigh-Taylor Turbulence, *Annu Rev Fluid Mech* **49**, 119 (2017).
- [16] O. Schilling, Progress on understanding Rayleigh–Taylor flow and mixing using synergy between simulation, modeling, and experiment, *J. Fluids Eng.* **142**, 120802 (2020).
- [17] A. Banerjee, Rayleigh-Taylor Instability: A status review of experimental designs and measurement diagnostics, *J. Fluids Eng.* **142**, 120801 (2020).
- [18] S. Atzeni and J. Meyer-ter-Vehn, *The Physics of Inertial Fusion: Beam Plasma Interaction, Hydrodynamics, Hot Dense Matter* (Clarendon Press, Oxford, UK, 2004).
- [19] J. D. Lindl, *Inertial Confinement Fusion: The Quest for Ignition and Energy Gain Using Indirect Drive* (Springer, Berlin, 1998).
- [20] D. Aslangil and M. L. Wong, Study of iso-thermal stratification strength on 2D multi-mode compressible Rayleigh-Taylor instability, presented at the *AIAA SCITECH 2022 Forum, San Diego, CA* (AIAA, Reston, VA, 2022), Paper No. 2022-0456.
- [21] S. F. Gull, The X-ray, optical and radio properties of young supernova remnants, *Mon. Not. R. Astron. Soc.* **171**, 263 (1975).
- [22] S. A. Colgate and R. H. White, The hydrodynamic behavior of supernova explosions, *Astrophys. J.* **143**, 626 (1966).
- [23] T. Ebisuzaki, T. Shigezumi, and K. i. Nomoto, Rayleigh-Taylor instability and mixing in SN 1987A, *Astrophys. J.* **344**, L65 (1989).
- [24] G. Dimonte, P. Ramaprabhu, and M. J. Andrews, Rayleigh-Taylor instability with complex acceleration history, *Phys. Rev. E* **76**, 046313 (2007).
- [25] P. Ramaprabhu, V. Karkhanis, and A. G. W. Lawrie, The Rayleigh-Taylor instability driven by an accel-decel-accel profile, *Phys. Fluids* **25**, 115104 (2013).
- [26] G. Dimonte and M. Schneider, Turbulent Rayleigh-Taylor instability experiments with variable acceleration, *Phys. Rev. E* **54**, 3740 (1996).
- [27] D. Aslangil, A. Banerjee, and A. G. W. Lawrie, Numerical investigation of initial condition effects on Rayleigh-Taylor instability with acceleration reversals, *Phys. Rev. E* **94**, 053114 (2016).
- [28] D. Aslangil, D. Livescu, and A. Banerjee, Acceleration reversal effects on buoyancy-driven homogeneous variable-density turbulence, presented at the *Proceedings of 22nd Australasian Fluid Mechanics Conference AFMC2020, Brisbane, Australia, 7-10 December 2020* (The University of Queensland, Brisbane, Australia).

- [29] D. Aslangil, Z. Farley, A. G. W. Lawrie, and A. Banerjee, Rayleigh–Taylor instability with varying periods of zero acceleration, *J. Fluids Eng.* **142**, 121103 (2020).
- [30] D. Livescu, T. Wei, and M. R. Petersen, Rayleigh–Taylor instability with gravity reversal, *Physica D* **417**, 132832 (2021).
- [31] D. Aslangil, D. Livescu, and A. Banerjee, Variable Density Mixing under Variable Mean Pressure Gradient, presented at the 15th European Turbulence Conference, Delft, The Netherlands, 2015.
- [32] G. Boffetta, M. Magnani, and S. Musacchio, Suppression of Rayleigh–Taylor turbulence by time-periodic acceleration, *Phys. Rev. E* **99**, 033110 (2019).
- [33] A. Banerjee and M. J. Andrews, 3-D Simulations to investigate initial condition effects on the growth of Rayleigh–Taylor mixing, *Int. J. Heat Mass Transfer* **52**, 3906 (2009).
- [34] G. Dimonte, D. L. Youngs, A. Dimits, S. Weber, M. Marinak, S. Wunsch, C. Garasi, A. Robinson, M. J. Andrews, P. Ramaprabhu, A. C. Calder, B. Fryxell, J. Biello, L. Dursi, P. MacNeice, K. Olson, P. Ricker, R. Rosner, F. Timmes, H. Tufo, Y. N. Young, and M. Zingale, A comparative study of the turbulent Rayleigh–Taylor (RT) instability using high-resolution 3D numerical simulations: The Alpha-Group collaboration, *Phys. Fluids* **16**, 1668 (2004).
- [35] O. Schilling, Self-similar Reynolds-averaged mechanical-scalar turbulence models for Rayleigh–Taylor, Richtmyer–Meshkov, and Kelvin–Helmholtz instability-induced mixing in the small Atwood number limit, *Phys. Fluids* **33**, 085129 (2021).
- [36] G. Dimonte and M. Schneider, Density ratio dependence of Rayleigh–Taylor mixing for sustained and impulsive acceleration histories, *Phys. Fluids* **12**, 304 (2000).
- [37] A. G. W. Lawrie and S. B. Dalziel, Turbulent diffusion in tall tubes, Part I: Models for Rayleigh Taylor instability, *Phys. Fluids* **23**, 085109 (2011).
- [38] P. Ramaprabhu, V. Karkhanis, R. Banerjee, H. Varsochi, M. Khan, and A. G. W. Lawrie, Evolution of the single-mode Rayleigh–Taylor instability under the influence of time-dependent accelerations, *Phys. Rev. E* **93**, 013118 (2016).
- [39] J. T. Horne and A. G. W. Lawrie, Aspect-ratio-constrained Rayleigh–Taylor instability, *Physica D* **406**, 132442 (2020).
- [40] A. G. W. Lawrie, Rayleigh–Taylor mixing: Confinement by stratification and geometry, Ph.D. dissertation, University of Cambridge, 2010.
- [41] T. E. Dobra, A. G. W. Lawrie, and S. B. Dalziel, The magic carpet: An arbitrary spectrum wave maker for internal waves, *Exp. Fluids* **60**, 172 (2019).
- [42] M. J. Andrews, Accurate computation of convective transport in transient two-phase flow, *Int. J. Numer. Methods Fluids* **21**, 205 (1995).
- [43] P. J. Schmid, Dynamic mode decomposition of numerical and experimental data, *J. Fluid Mech.* **656**, 5 (2010).
- [44] S. B. Pope, *Turbulent Flows* (Cambridge University Press, New York, 2000).
- [45] Y. Zhou and W. H. Cabot, Time-dependent study of anisotropy in Rayleigh–Taylor instability induced turbulent flows with a variety of density ratios, *Phys. Fluids* **31**, 084106 (2019).
- [46] N. Pal, S. Kurien, T. Clark, D. Aslangil, and D. Livescu, Two-point spectral model for variable-density homogeneous turbulence, *Phys. Rev. Fluids* **3**, 124608 (2018).
- [47] A. Banerjee, R. A. Gore, and M. J. Andrews, Development and validation of a turbulent-mix model for variable-density and compressible flows, *Phys. Rev. E* **82**, 046309 (2010).
- [48] D. Livescu, J. R. Ristorcelli, R. A. Gore, S. H. Dean, W. H. Cabot, and A. W. Cook, High-Reynolds number Rayleigh–Taylor turbulence, *J. Turbul.* **10**, N13 (2009).
- [49] B. R. Sutherland, *Internal Gravity Waves* (Cambridge University Press, Cambridge, UK, 2010).
- [50] T. E. Dobra, A. G. W. Lawrie, and S. B. Dalziel, Harmonics from a magic carpet, *J. Fluid Mech.* **911**, A29 (2021).
- [51] T. E. Dobra, A. G. W. Lawrie, and S. B. Dalziel, A hierarchical decomposition of internal wave fields, *J. Fluid Mech.* **934**, A33 (2022).